

Enhancing 3D Lane Detection and Topology Reasoning with 2D Lane Priors

Han Li¹, Zehao Huang², Zitian Wang¹, Wenge Rong¹, Naiyan Wang², and Si Liu¹

¹ Beihang University

² TuSimple

{bryce18373631, zehaohuang18, a2394797795, winsty}@gmail.com
{w.rong, liusi}@buaa.edu.cn

Abstract. 3D lane detection and topology reasoning are essential tasks in autonomous driving scenarios, requiring not only detecting the accurate 3D coordinates on lane lines, but also reasoning the relationship between lanes and traffic elements. Current vision-based methods, whether explicitly constructing BEV features or not, all establish the lane anchors/queries in 3D space while ignoring the 2D lane priors. In this study, we propose Topo2D, a novel framework based on Transformer, leveraging 2D lane instances to initialize 3D queries and 3D positional embeddings. Furthermore, we explicitly incorporate 2D lane features into the recognition of topology relationships among lane centerlines and between lane centerlines and traffic elements. Topo2D achieves 44.5% OLS on multi-view topology reasoning benchmark OpenLane-V2 and 62.6% F-Socre on single-view 3D lane detection benchmark OpenLane, exceeding the performance of existing state-of-the-art methods. The codes are released at <https://github.com/homothetic/Topo2D>.

Keywords: Autonomous Driving · 3D Lane Detection · Topology Reasoning

1 Introduction

3D lane detection, which focuses on detecting the accurate location of lanes, is one of the key components in the applications of the Advanced Driver Assistance System (ADAS). With the development and advancement of ADAS technology, the emergence of higher-level assisted driving functions, such as Navigate on Autopilot, has gradually shifted the demand for lane perception from 3D lane detection to the online High-Definition (HD) map construction [7, 12, 16, 17, 20]. In addition to detecting lane segments, online HD map construction also requires the identification of other static traffic elements, such as traffic lights and road signs, and requires the topology between lane segments themselves as well as between lanes and traffic elements [13, 35].

No matter for 3D lane detection task or online HD map construction, detecting 3D lanes is a critical component. Recent vision-based methods for lane

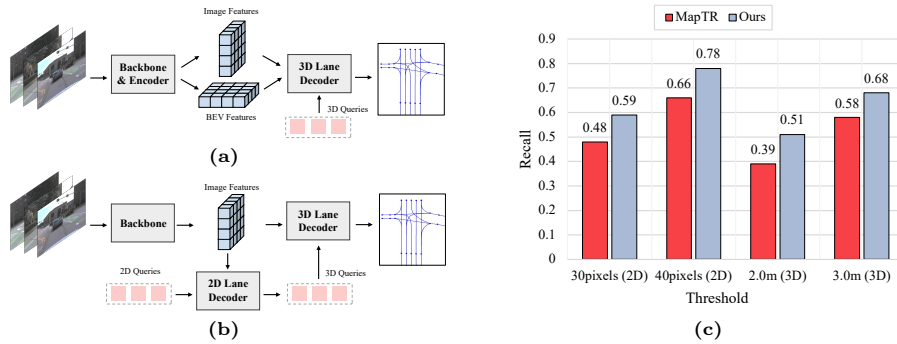


Fig. 1: (a) Previous methods randomly initialize 3D lane queries in 3D space. (b) Our method initializes 3D lane queries given 2D lane priors. (c) Comparison of lane detection recall under different thresholds. In both 2D recall and 3D recall, our model shows marked advancement relative to baseline MapTR [16] across various thresholds.

detection can be mainly grouped into two categories. The first stream focuses on preserving 2D image features, leveraging interactions between predefined 3D lane anchors (or queries) and 2D features for the final predictions [11, 22, 38]. For example, Anchor3DLane [11] initializes various 3D lane anchors and projects them onto 2D features using camera parameters, subsequently extracting features through bilinear interpolation. Other methods, such as MapTR [16], explicitly construct bird’s-eye-view (BEV) features [5, 8, 9, 13, 16, 36]. They define 3D lane queries in the same BEV space and employ attention mechanisms [15, 41] for feature aggregation.

Though these methods have achieved remarkable performances, they all establish the lane anchors in 3D space while ignoring the 2D lane priors. In this paper, we propose a new framework that leverages 2D lane priors to enhance the performance of lane detection. As shown in Fig. 1a and Fig. 1b, instead of adopting 3D queries initialized in 3D space, we utilize the 2D lane instances obtained by a 2D lane decoder as 3D queries. This strategy is motivated by an observation: lane detection within the 2D image space generally results in a higher recall than detection in 3D. We conduct experiments on the OpenLane-V2 [35] dataset, comparing the recall of MapTR and our method in both 2D and 3D spaces. Our findings, illustrated in Fig. 1c, demonstrate that detecting 2D lanes in image space directly achieves 12% (78% vs. 66%) higher recall than MapTR³. By integrating 2D priors, our method achieves a superior 3D recall compared to MapTR.

The benefit of involving 2D lane priors is also proven in the task of topology reasoning. Existing methods [13, 38] usually take two 3D queries and infer the topology structures through the concatenated features of them. However, on the one hand, the positional relationships of 2D lanes provide additional information

³ For 2D recall, we project 3D Ground Truth and the prediction of MapTR into the image space for evaluation.

for establishing topological relationships between 3D lanes. On the other hand, since traffic elements are detected in images, the topology prediction of lanes and traffic elements requires the incorporation of 2D lane positions. In our framework, we explicitly incorporate 2D lane features into the prediction of topology relationships.

Our framework, named Topo2D, enhances both lane detection and topology reasoning capabilities by integrating 2D lane priors. The 2D and 3D lane detectors are with similar transformer-based [34] architectures. For 3D lane detection, we use the 2D lane query features and 2D coordinates obtained by the 2D lane decoder to initialize the 3D lane queries and positional embeddings. For topology prediction, we utilize a comprehensive approach that not only involves the features from 3D lanes and traffic elements, but also integrates corresponding 2D lane features, thereby enhancing overall performance.

In summary, our contributions can be outlined as follows:

- We propose to initialize 3D lane queries and positional embeddings using 2D lane priors, thereby enhancing 3D lane perception performance.
- We explicitly utilize 2D lane information to assist the model in better recognizing the topology relationships among lane centerlines and between lane centerlines and traffic elements.
- We validate our Topo2D on the multi-view topology reasoning benchmark OpenLane-V2 [35] and the single-view 3D lane detection benchmark OpenLane [5]. Topo2D achieves state-of-the-art performance on both benchmarks.

2 Related Work

2.1 Lane Detection

The objective of 2D lane detection is to identify the precise location of lanes in 2D images. Among various methods [14, 28, 33] developed for 2D lane detection, anchor-based approaches have risen to prominence for their simplicity and efficiency. LineCNN [14] first proposes a novel representation method for lane anchors and achieving end-to-end lane detection. Then, LaneATT [33] develops anchor-based attention mechanism to gather global information. CLRNet [39] iteratively refines initial anchors through feature pyramids.

Building upon 2D lane detection, 3D lane detection predicts the 3D spatial coordinates of lanes. Early methods attempt to convert 2D image features into BEV features based on the assumption of flat ground. 3D-LaneNet [8] utilizes Inverse Perspective Mapping (IPM) to transform image features and then regresses lane segments on the resulted BEV feature map. Gen-LaneNet [9] introduces virtual top view based on IPM to achieve better perspective transformation.

However, flat ground assumption fails when encountering uphill/downhill scenarios, which are common in real-world driving scenes. To remedy this issue, PersFormer [5] employs Perspective Transformer to construct more robust BEV features. Anchor3DLane [11] defines anchor lines in 3D space and aggregates image features of lanes based on camera parameters, directly predicting the 3D

lane lines. LATR [25] adds 3D positional embeddings to the images, constructing image features that include 3D information, and designs lane-aware queries to extract 3D features from the images.

2.2 High Definition (HD) Map Construction

Multi-view-based online HD map construction can be regarded as an extension of the single-view-based 3D lane detection. In addition to detecting lanes, it also requires other static semantic elements in surrounding environment, such as pedestrian crossings and road boundaries. Conventionally HD map is constructed offline with SLAM-based methods [29,30]. With the advancement in BEV representation learning, recent studies [6,27,40] focus on predicting rasterized maps through BEV semantic segmentation. However, compared to vectorized maps, rasterized maps lack crucial instance-level information, such as lane structure, which is essential for downstream tasks.

For constructing vectorized HD maps, HDMapNet [12] follows a semantic segmentation-based approach. After generating BEV feature maps and obtaining the segmentation results of map elements, HDMapNet distinguishes different instances through post-processing. To pursue an end-to-end approach, VectorMapNet [20] models irregular map elements as a series of keypoints and predicts ordered point sets through a polyline generator. MapTR [16] and MapTRv2 [17] represent each map element as a set of equivalently arranged points. They propose hierarchical queries to simplify the task into a parallel regression problem.

Unlike these methods that define anchors or queries in 3D space for 3D lane perception, our Topo2D defines queries in 2D space and utilizes 2D priors such as lane features and lane coordinates to assist the 3D lane detector. Thanks to the 2D priors, the 3D lane detector learns more comprehensive image features, resulting in enhanced performance.

2.3 Topology Reasoning

With the introduction of the OpenLane-V2 [35] dataset, topology reasoning in driving scenes has attracted increasing attention. This task involves recognizing the topologies among lanes and lanes with traffic elements (e.g., traffic lights and road signs). TopoNet [13] employs a graph module to model the relationships after separately detecting centerlines and traffic elements, refining the shape and position of lanes using adjacent lanes and relevant traffic elements. TopoMLP [38] abandons complex graph neural networks and instead employs simple Multilayer Perceptrons (MLPs) to predict the relationships. Different from previous work, in order to achieve better consistency with more reliable 2D detection results, our Topo2D not only utilizes 3D lane features but also explicitly incorporates 2D lane features for topology relationship prediction.

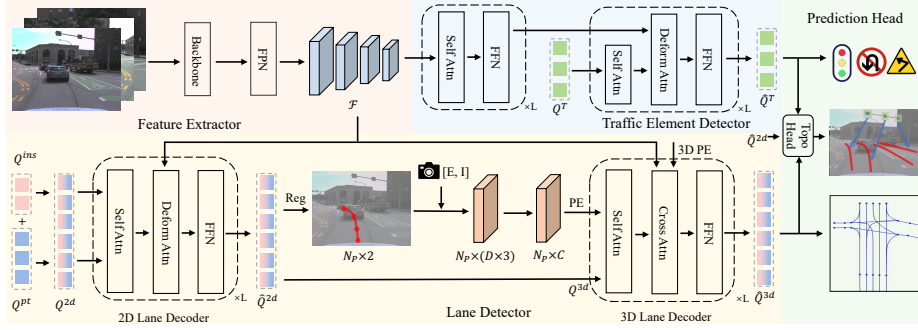


Fig. 2: The overall architecture of Topo2D. Given multi-view images, the images are first input to backbone network and FPN to extract image features. The image features are then fed into the subsequent 2D lane detector and 2D traffic element detector. The 3D lane detector initializes 3D lane queries and 3D position embeddings based on 2D lane priors and outputs 3D lane detection results. Finally, the 2D lane features are fused with the 3D lane features, and their relationships are estimated based on fused lane features and traffic element features.

3 Method

3.1 Overview

Fig. 2 shows the overall architecture of the proposed Topo2D. Topo2D can solve multiple tasks within a single pipeline, including lane detection, traffic element detection, lane-to-lane topology prediction, and lane-to-traffic element topology prediction.

Given multi-view images $\mathcal{I} = \{\mathbf{I}_i \in \mathbb{R}^{3 \times H_I \times W_I} | i = 1, 2, \dots, N_I\}$ from N_I camera views, the images are input to the backbone network (e.g., ResNet-50 [10]) and FPN [18] to extract multi-view multi-level 2D features $\mathcal{F} = \{\mathbf{F}_i^v \in \mathbb{R}^{C \times H_F^v \times W_F^v} | i = 1, 2, \dots, N_I; v = 1, 2, \dots, V\}$, where V is the number of FPN levels. The lane detector consists of two stages, 2D lane detection and 3D lane detection, and finally outputs a fixed number of 3D lane instances $\{\mathbf{L}_i \in \mathbb{R}^{N_P \times 3} | i = 1, 2, \dots, l\}$, where N_P is the point number of each instance. The traffic element detector is based on Deformable DETR [41], which generates 2D bounding boxes of traffic elements $\{\mathbf{T}_i \in \mathbb{R}^4 | i = 1, 2, \dots, t\}$ from the front camera view. MLP-based topology prediction head receives features extracted by the detectors to predict the connectivity $\mathbf{G}^{ll} \in \mathbb{R}^{l \times l}$ among lanes and indication relationships $\mathbf{G}^{lt} \in \mathbb{R}^{l \times t}$ between traffic elements and lanes. The details will be described in the following sections.

3.2 Lane Detector

In Topo2D, the 2D lane detector is first applied to each image to localize lane instances in the perspective views. Based on the detection results, we initialize

3D lane queries which comprise appearance features and positional embeddings derived from 2D lanes. The appearance features are generated from 2D lane features and the positional embeddings are initialized from 2D lane coordinates. These lane-related geometric and semantic information help better associate relevant features in the subsequent self-attention and cross-attention modules. The 3D lane detection part is built with a DETR-style [4] decoder, where the 3D lane queries interact with image features and output 3D lane coordinates after query updates.

2D Lane Detection. We denote a 2D lane $\mathbf{L}_i^{2d} \in \mathbb{R}^{N_P \times 2}$ as N_P points along side the 2D lane. In each camera view, we define a set of instance-level queries $\{\mathbf{Q}_i^{ins}\}_{i=1}^{N_L}$ and a set of point-level queries $\{\mathbf{Q}_j^{pt}\}_{j=1}^{N_P}$, following the practice of MapTR [16]. So all lanes can be represented as a set of hierarchical queries $\mathbf{Q}^{2d} = \{\mathbf{Q}_{ij}^{2d} | i = 1, \dots, N_L; j = 1, \dots, N_P\}$, where:

$$\mathbf{Q}_{ij}^{2d} = \mathbf{Q}_i^{ins} + \mathbf{Q}_j^{pt}. \quad (1)$$

Within each 2D lane decoder layer, the hierarchical queries go through a self-attention module, a cross-attention module, and a feed-forward network sequentially to update features. In the self-attention module, we adopt vanilla multi-head attention [34] to exchange information among hierarchical queries. In the cross-attention module, we adopt multi-scale deformable attention [41] to aggregate information from extracted image features. This process can be formulated as:

$$\mathbf{X} = \text{LN}(\text{MultiHeadAttn}(\mathbf{Q}^{2d}, \mathbf{P}^{2d})) + \mathbf{Q}^{2d}, \quad (2)$$

$$\hat{\mathbf{X}} = \text{LN}(\text{MSDeformAttn}(\mathbf{X}, \mathbf{F})) + \mathbf{X}, \quad (3)$$

$$\hat{\mathbf{Q}}^{2d} = \text{LN}(\text{FFN}(\hat{\mathbf{X}})) + \hat{\mathbf{X}}, \quad (4)$$

where \mathbf{P}^{2d} is 2D positional embedding as used in DETR [4].

The prediction heads consist of a classification branch and a point regression branch. The classification branch predicts the probability of the lane instance belonging to a specific class:

$$\mathbf{S}_i^{2d} = \text{Linear}(\text{AvgPooling}(\{\hat{\mathbf{Q}}_{ij}^{2d}\}_{j=1}^{N_P})), \quad (5)$$

and the point regression branch predicts the 2D coordinates of lane points $\mathbf{L}_i^{2d} = \{\mathbf{L}_{ij}^{2d}\}_{j=1}^{N_P} \in \mathbb{R}^{N_P \times 2}$ in the image space:

$$\mathbf{L}_{ij}^{2d} = \text{Linear}(\hat{\mathbf{Q}}_{ij}^{2d}). \quad (6)$$

3D Lane Query Initialization. We directly use the updated 2D lane features $\hat{\mathbf{Q}}^{2d}$ after the 2D lane decoder as the appearance features \mathbf{Q}^{3d} of the 3D lane queries. Additionally, we generate 3D positional embeddings based on the predicted 2D lane coordinates. Specifically, we use a camera ray to represent each

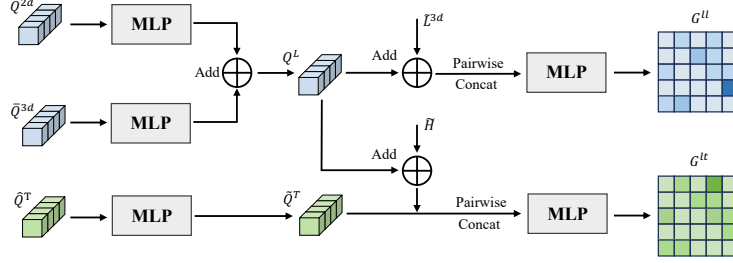


Fig. 3: Illustration of topology prediction heads. First, we embed the 2D lane instance queries using MLPs, and add them with the embedded 3D lane instance queries. Then we concatenate the lane queries with each other in pairs, as well as the lane queries with the traffic element queries in pairs, to predict the topology relationships. Additionally, for lane-lane topology, we incorporate embeddings of the 3D coordinates of lane points, while for lane-traffic element topology, we incorporate embeddings of camera parameters.

2D lane point in the 3D coordinate system. Following PETR [21], the camera rays are discretized to generate a set of points, where each point can be represented as $\mathbf{p}_{ijk}^{cam} = (u_{ij} \times d_k, v_{ij} \times d_k, d_k)$. (u_{ij}, v_{ij}) is the 2D lane point coordinate in the image space and $\{d_k\}_{k=1}^D$ are the pre-defined depth values along the axis orthogonal to the image plane. \mathbf{p}_{ijk}^{cam} in the camera coordinate system is then transformed to \mathbf{p}_{ijk} in the world coordinate system using camera parameters. Finally, we concatenate \mathbf{p}_{ijk} and feed them into an MLP to produce 3D positional embeddings:

$$\mathbf{P}_{ij}^{3d} = \text{MLP}(\text{Concat}(\{\mathbf{p}_{ijk}\}_{k=1}^D)). \quad (7)$$

3D Lane Detection. Given the appearance features \mathbf{Q}^{3d} and positional embeddings \mathbf{P}^{3d} of 3D lane queries, the 3D lane detector iteratively refines the appearance features. The structure of 3D lane detector is similar to the 2D counterpart, but the cross-attention module is implemented with a global multi-head attention to aggregate 3D lane features:

$$\mathbf{Y} = \text{LN}(\text{MultiHeadAttn}(\mathbf{Q}^{3d}, \mathbf{P}^{3d})) + \mathbf{Q}^{3d}, \quad (8)$$

$$\hat{\mathbf{Y}} = \text{LN}(\text{MultiHeadAttn}(\mathbf{Y}, \mathbf{F})) + \mathbf{Y}, \quad (9)$$

$$\hat{\mathbf{Q}}^{3d} = \text{LN}(\text{FFN}(\hat{\mathbf{Y}})) + \hat{\mathbf{Y}}. \quad (10)$$

Then, similar to Eq. (5) and Eq. (6), the prediction heads predict instance class score \mathbf{S}_i^{3d} and 3D coordinates $\mathbf{L}_i^{3d} = \{\mathbf{L}_{ij}^{3d}\}_{j=1}^{N_P} \in \mathbb{R}^{N_P \times 3}$ based on $\hat{\mathbf{Q}}^{3d}$.

3.3 Topology Reasoning

We use deformable DETR [41] as the traffic element detector to output bounding boxes and corresponding features $\{\hat{\mathbf{Q}}_i^T\}_{i=1}^t$ of the traffic elements in the front

view. After obtaining lane and traffic element detection results, 2D lane information is explicitly incorporated in this process to boost the performance of topology inference.

On one hand, 2D lane segments significantly contribute to the inference of the connectivity among lane instances. On the other hand, since traffic elements are inherently captured in the image space, 2D lane information facilitates more accurate alignments with traffic element information.

Specifically, we first utilize average pooling operation to convert hierarchical queries into instance queries $\{\bar{\mathbf{Q}}_i^{3d}\}_{i=1}^l$ and $\{\bar{\mathbf{Q}}_i^{2d}\}_{i=1}^l$, where $l = N_I \times N_L$. After that, we embed the 2D lane queries using MLPs and add them with embed 3D lane queries:

$$\mathbf{Q}_i^L = \text{MLP}(\bar{\mathbf{Q}}_i^{3d}) + \text{MLP}(\bar{\mathbf{Q}}_i^{2d}). \quad (11)$$

Then, we also embed the 3d lane coordinates \mathbf{L}_i^{3d} using MLPs:

$$\tilde{\mathbf{L}}_i^{3d} = \text{MLP}(\text{Flatten}(\mathbf{L}_i^{3d})). \quad (12)$$

As illustrated in Fig. 3, the lane-lane topology reasoning branch predicts the connection among 3D lanes:

$$\mathbf{G}_{mn}^{ll} = \text{MLP}(\text{Concat}(\mathbf{Q}_m^L + \tilde{\mathbf{L}}_m^{3d}; \mathbf{Q}_n^L + \tilde{\mathbf{L}}_n^{3d})), \quad (13)$$

where \mathbf{Q}_m^L , $\tilde{\mathbf{L}}_m^{3d}$ and \mathbf{Q}_n^L , $\tilde{\mathbf{L}}_n^{3d}$ denote the features and coordinate embeddings of the m^{th} and n^{th} lane. The lane-traffic element topology reasoning branch predicts the topology relationship between 3D lanes and traffic elements:

$$\tilde{\mathbf{H}} = \text{MLP}(\text{Flatten}(\mathbf{H}[: 3, :])), \quad (14)$$

$$\mathbf{G}_{mn}^{lt} = \text{MLP}(\text{Concat}(\mathbf{Q}_m^L + \tilde{\mathbf{H}}; \text{MLP}(\hat{\mathbf{Q}}_n^T))), \quad (15)$$

where \mathbf{H} denotes a standard 4×4 transformation matrix between 3D world coordinate system and 2D image coordinate system. \mathbf{Q}_m^L and $\hat{\mathbf{Q}}_n^T$ denote the features of the m^{th} lane and n^{th} traffic element, respectively.

3.4 Loss Function

Our total loss function is defined as follows:

$$\mathcal{L}_{\text{total}} = \mathcal{L}_{\text{2d-lane}} + \mathcal{L}_{\text{3d-lane}} + \mathcal{L}_t + \mathcal{L}_{\text{topo-ll}} + \mathcal{L}_{\text{topo-lt}}, \quad (16)$$

where $\mathcal{L}_{\text{2d-lane}}$ and $\mathcal{L}_{\text{3d-lane}}$ are lane detection losses. Both of them adopt the focal loss [19] for classification and \mathcal{L}_1 loss for lane points regression. \mathcal{L}_t is traffic element detection loss, including focal loss, \mathcal{L}_1 loss and GIoU loss. The lane-lane topology loss $\mathcal{L}_{\text{topo-ll}}$ and lane-traffic topology loss $\mathcal{L}_{\text{topo-lt}}$ are focal losses for binary classification. We omit the weight for each loss for brevity. The details are presented in the supplementary materials.

4 Experiments

4.1 Datasets and Metrics

To evaluate the proposed method, we conduct experiments on two benchmarks: the multi-view topology reasoning benchmark OpenLane-V2 [35] and the single-view 3D lane detection benchmark OpenLane [5].

OpenLane-V2 [35] is a large-scale perception and reasoning dataset for driving scenes. It comprises two subsets, *subset_A* and *subset_B*, developed from Argoverse2 [37] and nuScenes [2] respectively. We utilize only *subset_A* due to the lack of height information in *subset_B*. OpenLane-V2 *subset_A* comprises 1000 scenes annotated at 2Hz, with each frame containing images from 7 views.

The evaluation metrics consist of four components: DET_l and DET_t measure the instance-level performance of centerline and traffic element using mean average precision (mAP). Specifically, DET_l employs the Fréchet distance to quantify similarity, averaging over matching thresholds set at $\{1.0m, 2.0m, 3.0m\}$, while DET_t employs Intersection over Union (IoU) and computes the average over different traffic categories. For topology reasoning metrics, TOP_{ll} and TOP_{lt} are mAP metrics adapted from the graph domain⁴. To evaluate the overall effect of detection and topology reasoning, the OpenLane-V2 Score (OLS) is computed as follows:

$$OLS = \frac{1}{4}[DET_l + DET_t + f(TOP_{ll}) + f(TOP_{lt})], \quad (17)$$

where f is a scale function to emphasize the task of topology reasoning.

In addition, to better evaluate the lane detection results and compare them with previous lane detection methods, OpenLane-V2 [35] also provides a lane related metric $DET_{l, chamfer}$, which utilizes the Chamfer distance as the similarity measure and computes average over matching thresholds set at $\{0.5m, 1.0m, 1.5m\}$.

OpenLane [5] is a 3D lane detection benchmark constructed upon the Waymo open dataset [32]. This dataset comprises 1000 segments, consisting of 200K frames. Each frame contains only front view images with a resolution of 1280×1920 . OpenLane includes 880K lane annotations distributed across 14 categories.

During the evaluation process, predictions and ground-truths are matched via minimum cost flow, where pairwise costs are defined as the square root of the sum of squared point-to-point distances. A prediction is considered true positive (TP) if more than 75% of the predicted points are within a distance threshold (i.e., 1.5m) from the ground-truth points. Based on this definition, the maximum F1 score is further computed, and x/z errors are calculated separately for

⁴ The metrics for TOP scores have been updated. We use the updated metrics in our evaluation as suggested by OpenLane-V2.

Table 1: Comparison on topology reasoning task on OpenLane-V2 *subset_A*. The reported results of state-of-art methods are from TopoNet [13].

Method	Backbone	Epoch	OLS \uparrow	DET _l \uparrow	DET _t \uparrow	TOP _{ul} \uparrow	TOP _{tl} \uparrow
STSU [3]	ResNet-50	24e	29.3	12.7	43.0	2.9	19.8
VectorMapNet [20]	ResNet-50	24e	24.9	11.1	41.7	2.7	9.2
MapTR [16]	ResNet-50	24e	31.0	17.7	43.5	5.9	15.1
TopoNet [13]	ResNet-50	24e	39.8	28.6	48.6	10.9	23.8
Topo2D (Ours)	ResNet-50	24e	44.5	29.1	50.6	22.3	26.2

Table 2: Comparison on centerline detection task without incorporating traffic elements on OpenLane-V2 *subset_A*.

Method	Trained w/. Topo	DET _l \uparrow	DET _{l, chamfer} \uparrow
VectorMapNet [20]	×	12.7	10.3
MapTR [16]	×	10.0	21.7
Topo2D (Ours)	×	26.6	31.0
STSU [3]	✓	14.2	13.8
TopoNet [13]	✓	27.7	27.4
Topo2D (Ours)	✓	28.8	32.4

near distance (0-40 meters) and far distance (40-100 meters). Additionally, category accuracy is reported, which computes the proportion of correctly predicted categories to all TP predictions.

4.2 Implementation Details

We use ResNet-50 [10] as backbone networks, followed by FPN [18] to generate multi-level features. In the lane detector, we set 20 instance queries and 11 point queries in each camera view. Both the 2D and 3D decoders contain 6 decoder layers. The 2D lane ground-truths are obtained by projecting 3D lane ground-truths to each view and cropping the visible parts of each lane. The loss weights for classification and regression are set to 2.0 and 5.0, respectively. We use Deformable DETR [41] as the traffic element detector. The loss weights for classification, regression, and GIoU are set to 2.0, 5.0 and 2.0. Both the topology reasoning branches comprise a three-layer MLP, with a loss weight set to 5.0. We use AdamW [24] optimizer with a weight decay rate of 0.01, and use the cosine annealing policy [23] for learning rate adjustment. HSV augmentation and grid mask [31] are used during training. All the experiments are conducted on eight A100 GPUs. More details are given in the supplementary materials.

4.3 Comparison on OpenLane-V2 Dataset

We first compare the performance on the topology reasoning task. Tab. 1 shows the results on OpenLane-V2 *subset_A*. Our Topo2D achieves 44.5% OLS when

Table 3: Comparison with state-of-art methods on OpenLane validation set. *Cate-Acc* represents category accuracy.

Method	F-Score \uparrow	Cate-Acc \uparrow	X-Near \downarrow	X-Far \downarrow	Z-Near \downarrow	Z-Far \downarrow
3D-LaneNet [8]	44.1	-	0.479	0.572	0.367	0.443
Gen-LaneNet [9]	32.3	-	0.593	0.494	0.140	0.195
PersFormer [5]	50.5	89.5	0.319	0.325	0.112	0.141
CurveFormer [1]	50.5	-	0.340	0.772	0.207	0.651
Anchor3DLane [11]	53.7	90.9	0.276	0.311	0.107	0.138
BEVLaneDet [36]	58.4	-	0.309	0.659	0.244	0.631
PETRV2 [22]	61.2	-	0.400	0.573	0.265	0.413
LATR [25]	61.9	92.0	0.219	0.259	0.075	0.104
Topo2D (Ours)	62.6	94.0	0.226	0.244	0.088	0.111

using ResNet-50 for training 24 epochs, surpassing other state-of-the-art methods. In terms of topology related metrics, compared to TopoNet, we achieve a 11.4% improvement in TOP_{ll} and a 2.4% improvement in TOP_{lt} .

It is noteworthy that some previous multi-view 3D lane detection methods choose to use Chamfer distance to evaluate the performance of unordered lane detection [16, 20]. To have a more comprehensive comparison, we also provide the comparison of centerline detection task under the same evaluation protocol, as marked by $DET_{l, chamfer}$ in Tab. 2. Topo2D achieves an improvement of 10.7% on $DET_{l, chamfer}$ compared to MapTR when training without topology prediction and an improvement of 5.0% compared to TopoNet with topology reasoning.

We further investigate why our method achieves a higher improvement on $DET_{l, chamfer}$ compared to DET_l . DET_l is based on Fréchet distance, treating the lane as a directed line, while $DET_{l, chamfer}$ uses the Chamfer distance, treating the lane as a set of points. DET_l is more sensitive to the position of each point, especially the starting point and the ending point. For instance, distant lanes (orange box in Fig. 4b) often occupy fewer pixels in the 2D image, which can cause predicted 3D lanes that align well with ground truths except for less precise starting/ending points. For those lanes, a Fréchet distance-based metric is easier to treat them as false positives compared to a Chamfer distance-based metric.

4.4 Comparison on OpenLane Dataset

We present the main results on OpenLane validation set in Tab. 3. Compared to the state-of-the-art method LATR, Topo2D achieves an improvement of 0.7% in F-Score and 2.0% in category accuracy with similar x/z errors (± 1.5 cm), demonstrating its performance in accurately detecting 3D lanes. We also provide the performance comparison under different scenarios in the supplementary materials.

Table 4: Ablation studies on OpenLane-V2 *subset_A*. All the experiments use ResNet-50 as backbone and train for 24 epochs.

2D Rand.				Num.			
	DET _l ↑	DET _{l,chamfer} ↑	TOP _{ll} ↑		DET _l ↑	DET _{l,chamfer} ↑	TOP _{ll} ↑
✓	24.7	28.8	19.1	10	21.4	25.9	12.9
✓	28.8	32.4	22.4	20	28.8	32.4	22.4
✓ ✓	26.8	31.7	22.0	30	27.8	31.8	21.3

(a) Initialization method for 3D queries.

Method				Query			
	DET _l ↑	DET _{l,chamfer} ↑	TOP _{ll} ↑		DET _l ↑	DET _{l,chamfer} ↑	TOP _{ll} ↑
2D	28.8	32.4	22.4	Ins.	25.8	30.1	21.2
3D	23.8	27.9	17.6	Hie.	28.8	32.4	22.4

(c) Design of 2D lane ground truths.

3D Proj.		2D OLS ↑		DET _l ↑ DET _t ↑ TOP _{ll} ↑ TOP _{lt} ↑			
✓		43.8	28.6	50.9	21.5	24.5	
✓	✓	44.1	28.8	50.7	21.8	25.3	
✓	✓ ✓	44.5	29.1	50.6	22.3	26.2	

(e) Impact of adding 2D information.

4.5 Ablation Study

In this section, we conduct ablation experiments on OpenLane-V2 *subset_A*. All the models are trained for 24 epochs with ResNet-50 [10] as backbone network. For modules specifically related to lane detection, we conduct experiments on centerline topology task without incorporating traffic elements, and compare the results on DET_l, DET_{l,chamfer} and TOP_{ll}.

Initialization method for 3D queries. To evaluate the effectiveness of the 2D-based initialization, we conduct experiments employing various initialization methods for 3D lane queries. As demonstrated in Tab. 4a, compared to random initialization in 3D space, our proposed 2D-based initialization method significantly enhances performance (28.8% vs. 24.7% on DET_l). Additionally, when mixing these two types of 3D lane queries while maintaining a constant number of queries, we observe a decline in performance. It is noted that 3D lane queries with random initialization tended to match only relatively simple instances, leaving the more complex instances to those queries initialized with 2D lane priors.

Number of instance queries. In Tab. 4b, we configure the number of instance queries for each view to be 10, 20, and 30, respectively. Given the large number of lanes present in complex intersection scenes, the model’s performance

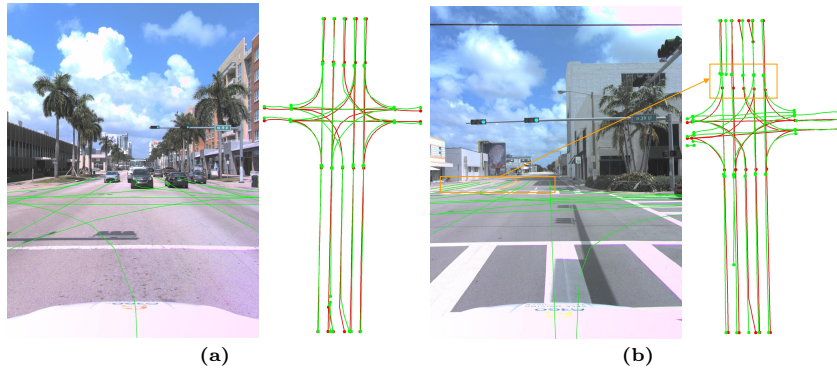


Fig. 4: Visualization of 2D and 3D lane detection results on OpenLane-V2 *subset_A*. (a) is an intersection scene and our method accurately detects the positions of all centerlines in this scene. (b) is a *failure case* where our method predicts centerlines that align well with ground truths except for less precise starting/ending points. Ground truths are showed in **red**, while predictions are showed in **green**. Best viewed in color.

declines when the query number is set to 10. Conversely, increasing the query number to 30 introduces a higher proportion of negative samples, which could negatively impact the training process, leading to slight performance degradation. Consequently, we set the query number to 20 as the default setting in our experiments.

Design of 2D lane ground-truths. Considering that instances in the 3D scene may not entirely appear within a single 2D view, we compare the performance under different designs for 2D lane ground-truths. When using the 2D sampling method, for each view, we project the visible parts of 3D lanes onto the image, and perform equidistant sampling on the image to generate 2D lane ground-truths. When using the 3D sampling method, we equidistantly sample the entire 3D lanes in the 3D space and project all points onto the image. The 2D lane detector not only detects the point coordinates but also predicts their visibility status in current view. The differences of these two methods are more notable in farther distance. Experimental results in Tab. 4c show that when using the 2D sample method, the training of the 2D lane detector is more stable, resulting in better detection performance.

Instance query vs. hierarchical query. Before detecting 3D lanes, we also attempt to fuse hierarchical 2D lane queries into instance 3D lane queries using MLPs:

$$\mathbf{Q}_i^{3d} = \text{MLP}(\text{Concat}(\{\hat{\mathbf{Q}}_{ij}^{2d}\}_{j=1}^{N_P})). \quad (18)$$

Each instance query predicts the coordinates of all points on this lane instance. In Tab. 4d, experiment results indicate that this fusion approach makes it difficult

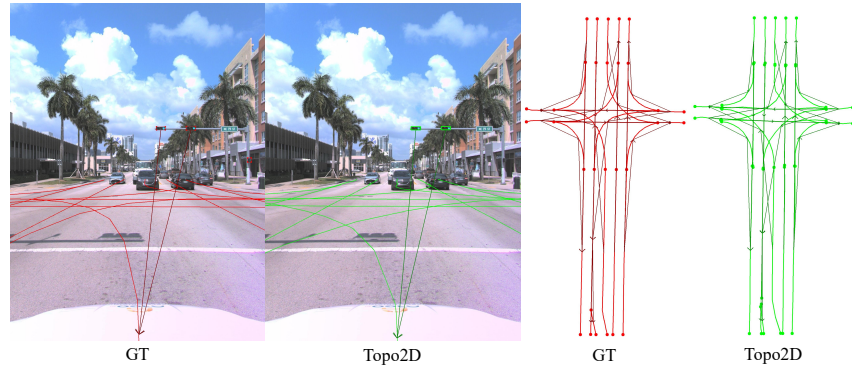


Fig. 5: Visualization of topology reasoning results on OpenLane-V2 *subset_A*. Left: Lane-traffic element topology. Right: Lane-lane topology. Ground truths are showed in **red**, while predictions are showed in **green**. Best viewed in color.

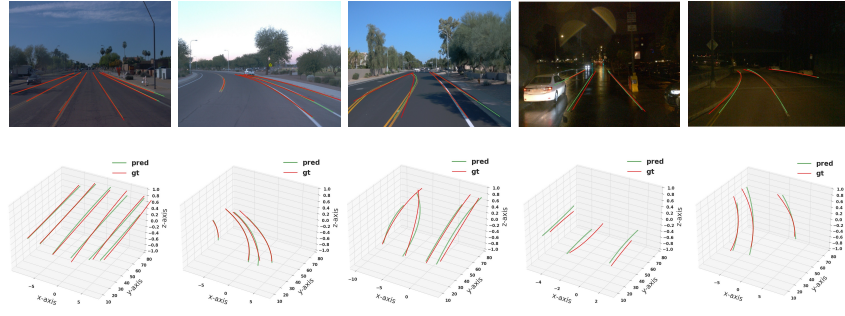


Fig. 6: Visualization under different scenarios on OpenLane validation set.

for the 3D lane instance queries to locate the corresponding image features during cross attention module, resulting in sub-optimal performance.

Impact of adding 2D information. We evaluate the impact of adding 2D information into the topology reasoning task. As illustrated in Tab. 4e, directly adding the projection matrix from 3D world coordinate to 2D image coordinate benefits the prediction of lane-traffic element topology. Introducing extra 2D query features results in further enhancements in both TOP_{ll} and TOP_{lt} , verifying the value of adding 2D information for effective topology reasoning.

4.6 Visualization

Fig. 4a and Fig. 5 show our lane detection and topology prediction results on OpenLane-V2 [35]. It can be observed that even in intersections without visual lane cues, our 2D lane detector still detect most of the centerlines, providing high-recall lane candidates for the 3D lane detector. We also visualize the results

on the OpenLane [5] dataset, as shown in Fig. 6. More qualitative results are included in the supplementary materials.

5 Conclusion

This paper proposes a new framework Topo2D for lane detection and topology reasoning. By initializing 3D lane queries based on 2D lane priors, the 3D lane detector learns more comprehensive image features, achieving higher detection recall rate. We further explicitly incorporate 2D lane features into the prediction of the topological structure. Experimental results show that our Topo2D outperforms previous state-of-the-art methods on multi-view topology reasoning benchmark OpenLane-V2 and single-view 3D lane detection benchmark OpenLane.

References

1. Bai, Y., Chen, Z., Fu, Z., Peng, L., Liang, P., Cheng, E.: Curveformer: 3d lane detection by curve propagation with curve queries and attention. In: 2023 IEEE International Conference on Robotics and Automation (ICRA). pp. 7062–7068. IEEE (2023)
2. Caesar, H., Bankiti, V., Lang, A.H., Vora, S., Liong, V.E., Xu, Q., Krishnan, A., Pan, Y., Baldan, G., Beijbom, O.: nuscenes: A multimodal dataset for autonomous driving. In: Proceedings of the IEEE/CVF conference on computer vision and pattern recognition. pp. 11621–11631 (2020)
3. Can, Y.B., Liniger, A., Paudel, D.P., Van Gool, L.: Structured bird’s-eye-view traffic scene understanding from onboard images. In: Proceedings of the IEEE/CVF International Conference on Computer Vision. pp. 15661–15670 (2021)
4. Carion, N., Massa, F., Synnaeve, G., Usunier, N., Kirillov, A., Zagoruyko, S.: End-to-end object detection with transformers. In: European conference on computer vision. pp. 213–229. Springer (2020)
5. Chen, L., Sima, C., Li, Y., Zheng, Z., Xu, J., Geng, X., Li, H., He, C., Shi, J., Qiao, Y., et al.: Persformer: 3d lane detection via perspective transformer and the openlane benchmark. In: European Conference on Computer Vision. pp. 550–567. Springer (2022)
6. Chen, S., Cheng, T., Wang, X., Meng, W., Zhang, Q., Liu, W.: Efficient and robust 2d-to-bev representation learning via geometry-guided kernel transformer. arXiv preprint arXiv:2206.04584 (2022)
7. Ding, W., Qiao, L., Qiu, X., Zhang, C.: Pivotnet: Vectorized pivot learning for end-to-end hd map construction. In: Proceedings of the IEEE/CVF International Conference on Computer Vision. pp. 3672–3682 (2023)
8. Garnett, N., Cohen, R., Pe’er, T., Lahav, R., Levi, D.: 3d-lanenet: end-to-end 3d multiple lane detection. In: Proceedings of the IEEE/CVF International Conference on Computer Vision. pp. 2921–2930 (2019)
9. Guo, Y., Chen, G., Zhao, P., Zhang, W., Miao, J., Wang, J., Choe, T.E.: Gen-lanenet: A generalized and scalable approach for 3d lane detection. In: Computer Vision–ECCV 2020: 16th European Conference, Glasgow, UK, August 23–28, 2020, Proceedings, Part XXI 16. pp. 666–681. Springer (2020)

10. He, K., Zhang, X., Ren, S., Sun, J.: Deep residual learning for image recognition. In: Proceedings of the IEEE conference on computer vision and pattern recognition. pp. 770–778 (2016)
11. Huang, S., Shen, Z., Huang, Z., Ding, Z.h., Dai, J., Han, J., Wang, N., Liu, S.: Anchor3dlane: Learning to regress 3d anchors for monocular 3d lane detection. In: Proceedings of the IEEE/CVF Conference on Computer Vision and Pattern Recognition. pp. 17451–17460 (2023)
12. Li, Q., Wang, Y., Wang, Y., Zhao, H.: Hdmapnet: An online hd map construction and evaluation framework. In: 2022 International Conference on Robotics and Automation (ICRA). pp. 4628–4634. IEEE (2022)
13. Li, T., Chen, L., Geng, X., Wang, H., Li, Y., Liu, Z., Jiang, S., Wang, Y., Xu, H., Xu, C., et al.: Topology reasoning for driving scenes. arXiv preprint arXiv:2304.05277 (2023)
14. Li, X., Li, J., Hu, X., Yang, J.: Line-cnn: End-to-end traffic line detection with line proposal unit. IEEE Transactions on Intelligent Transportation Systems **21**(1), 248–258 (2019)
15. Li, Z., Wang, W., Li, H., Xie, E., Sima, C., Lu, T., Qiao, Y., Dai, J.: Bevformer: Learning bird’s-eye-view representation from multi-camera images via spatiotemporal transformers. In: European conference on computer vision. pp. 1–18. Springer (2022)
16. Liao, B., Chen, S., Wang, X., Cheng, T., Zhang, Q., Liu, W., Huang, C.: Maptr: Structured modeling and learning for online vectorized hd map construction. arXiv preprint arXiv:2208.14437 (2022)
17. Liao, B., Chen, S., Zhang, Y., Jiang, B., Zhang, Q., Liu, W., Huang, C., Wang, X.: Maptrv2: An end-to-end framework for online vectorized hd map construction. arXiv preprint arXiv:2308.05736 (2023)
18. Lin, T.Y., Dollár, P., Girshick, R., He, K., Hariharan, B., Belongie, S.: Feature pyramid networks for object detection. In: Proceedings of the IEEE conference on computer vision and pattern recognition. pp. 2117–2125 (2017)
19. Lin, T.Y., Goyal, P., Girshick, R., He, K., Dollár, P.: Focal loss for dense object detection. In: Proceedings of the IEEE international conference on computer vision. pp. 2980–2988 (2017)
20. Liu, Y., Yuan, T., Wang, Y., Wang, Y., Zhao, H.: Vectormapnet: End-to-end vectorized hd map learning. In: International Conference on Machine Learning. pp. 22352–22369. PMLR (2023)
21. Liu, Y., Wang, T., Zhang, X., Sun, J.: Petr: Position embedding transformation for multi-view 3d object detection. In: European Conference on Computer Vision. pp. 531–548. Springer (2022)
22. Liu, Y., Yan, J., Jia, F., Li, S., Gao, A., Wang, T., Zhang, X.: Petrv2: A unified framework for 3d perception from multi-camera images. In: Proceedings of the IEEE/CVF International Conference on Computer Vision. pp. 3262–3272 (2023)
23. Loshchilov, I., Hutter, F.: Sgdr: Stochastic gradient descent with warm restarts. arXiv preprint arXiv:1608.03983 (2016)
24. Loshchilov, I., Hutter, F.: Decoupled weight decay regularization. arXiv preprint arXiv:1711.05101 (2017)
25. Luo, Y., Zheng, C., Yan, X., Kun, T., Zheng, C., Cui, S., Li, Z.: Latr: 3d lane detection from monocular images with transformer. In: Proceedings of the IEEE/CVF International Conference on Computer Vision. pp. 7941–7952 (2023)
26. Milletari, F., Navab, N., Ahmadi, S.A.: V-net: Fully convolutional neural networks for volumetric medical image segmentation. In: 2016 fourth international conference on 3D vision (3DV). pp. 565–571. Ieee (2016)

27. Pan, B., Sun, J., Leung, H.Y.T., Andonian, A., Zhou, B.: Cross-view semantic segmentation for sensing surroundings. *IEEE Robotics and Automation Letters* **5**(3), 4867–4873 (2020)
28. Qin, Z., Wang, H., Li, X.: Ultra fast structure-aware deep lane detection. In: *Computer Vision–ECCV 2020: 16th European Conference, Glasgow, UK, August 23–28, 2020, Proceedings, Part XXIV 16*. pp. 276–291. Springer (2020)
29. Shan, T., Englot, B.: Lego-loam: Lightweight and ground-optimized lidar odometry and mapping on variable terrain. In: *2018 IEEE/RSJ International Conference on Intelligent Robots and Systems (IROS)*. pp. 4758–4765. IEEE (2018)
30. Shan, T., Englot, B., Meyers, D., Wang, W., Ratti, C., Rus, D.: Lio-sam: Tightly-coupled lidar inertial odometry via smoothing and mapping. In: *2020 IEEE/RSJ international conference on intelligent robots and systems (IROS)*. pp. 5135–5142. IEEE (2020)
31. Singh, K.K., Yu, H., Sarmasi, A., Pradeep, G., Lee, Y.J.: Hide-and-seek: A data augmentation technique for weakly-supervised localization and beyond. *arXiv preprint arXiv:1811.02545* (2018)
32. Sun, P., Kretzschmar, H., Dotiwalla, X., Chouard, A., Patnaik, V., Tsui, P., Guo, J., Zhou, Y., Chai, Y., Caine, B., et al.: Scalability in perception for autonomous driving: Waymo open dataset. In: *Proceedings of the IEEE/CVF conference on computer vision and pattern recognition*. pp. 2446–2454 (2020)
33. Tabelini, L., Berriel, R., Paixao, T.M., Badue, C., De Souza, A.F., Oliveira-Santos, T.: Keep your eyes on the lane: Real-time attention-guided lane detection. In: *Proceedings of the IEEE/CVF conference on computer vision and pattern recognition*. pp. 294–302 (2021)
34. Vaswani, A., Shazeer, N., Parmar, N., Uszkoreit, J., Jones, L., Gomez, A.N., Kaiser, Ł., Polosukhin, I.: Attention is all you need. *Advances in neural information processing systems* **30** (2017)
35. Wang, H., Li, T., Li, Y., Chen, L., Sima, C., Liu, Z., Wang, B., Jia, P., Wang, Y., Jiang, S., et al.: Openlane-v2: A topology reasoning benchmark for unified 3d hd mapping. *Advances in Neural Information Processing Systems* **36** (2024)
36. Wang, R., Qin, J., Li, K., Li, Y., Cao, D., Xu, J.: Bev-lanedet: An efficient 3d lane detection based on virtual camera via key-points. In: *Proceedings of the IEEE/CVF Conference on Computer Vision and Pattern Recognition*. pp. 1002–1011 (2023)
37. Wilson, B., Qi, W., Agarwal, T., Lambert, J., Singh, J., Khandelwal, S., Pan, B., Kumar, R., Hartnett, A., Pontes, J.K., et al.: Argoverse 2: Next generation datasets for self-driving perception and forecasting. *arXiv preprint arXiv:2301.00493* (2023)
38. Wu, D., Chang, J., Jia, F., Liu, Y., Wang, T., Shen, J.: Topomlp: An simple yet strong pipeline for driving topology reasoning. *arXiv preprint arXiv:2310.06753* (2023)
39. Zheng, T., Huang, Y., Liu, Y., Tang, W., Yang, Z., Cai, D., He, X.: Clnet: Cross layer refinement network for lane detection. In: *Proceedings of the IEEE/CVF conference on computer vision and pattern recognition*. pp. 898–907 (2022)
40. Zhou, B., Krähenbühl, P.: Cross-view transformers for real-time map-view semantic segmentation. In: *Proceedings of the IEEE/CVF conference on computer vision and pattern recognition*. pp. 13760–13769 (2022)
41. Zhu, X., Su, W., Lu, L., Li, B., Wang, X., Dai, J.: Deformable detr: Deformable transformers for end-to-end object detection. *arXiv preprint arXiv:2010.04159* (2020)

Appendix

A More Implementation Details

For the 2D lane detector, in order to adapt to the arbitrary shape of 2D lanes, we add an edge direction loss [16] to supervise the geometrical shape with a loss weight set to 0.005. In addition, we add an auxiliary segmentation head to predict 2D lane instance masks on OpenLane [5] dataset. The segmentation loss is defined as:

$$\mathcal{L}_{\text{seg}} = \mathcal{L}_{\text{obj}} + \mathcal{L}_{\text{dice}} + \mathcal{L}_{\text{pixel}}, \quad (19)$$

where \mathcal{L}_{obj} , $\mathcal{L}_{\text{dice}}$ and $\mathcal{L}_{\text{pixel}}$ are binary cross entropy loss for the IoU-aware objectness, dice loss [26] and pixel-wise binary cross entropy loss for segmentation mask, respectively. The loss weights for \mathcal{L}_{obj} , $\mathcal{L}_{\text{dice}}$ and $\mathcal{L}_{\text{pixel}}$ are set to 1.0, 2.0 and 5.0. For the predictions of the lane detector and traffic element detector, we use bipartite matching to assign ground truths. This matching results are directly used for topology reasoning loss.

For the OpenLane-V2 dataset [35], the front view images are first cropped and padded to match the size of other views. Then all images are resized to 775×1024 with a scaling factor of 0.5. The batch size is 8 with an initial learning rate of $3e-4$. For the OpenLane [5] dataset, all input images are resized to 800×1024 . The structure of the lane detection model is similar to the centerline detection model used on OpenLane-V2 [35]. The batch size is 32 with an initial learning rate of $2e-4$.

Our 2D-based initialization method utilizes a 6-layer 2D lane decoder and a 6-layer 3D lane decoder. In the ablation experiments exploring various initialization methods for 3D lane queries, to ensure fairness in comparison, we set the 3D lane decoder to 12 layers when employing the random initialization method.

B Quantitative Results

B.1 Comparison on OpenLane-V2 Dataset

We provide the performance of topology reasoning task using metrics before updating. As depicted in Tab. 5, our method achieves 37.8% OLS, indicating a 2.2% improvement compared to TopoNet [13].

B.2 Comparison on OpenLane Dataset

We provide the performance comparison under different scenarios in Tab. 6. Topo2D outperforms LATR [25] across most scenarios. Specifically, we observe that our model performs more accurate lane detection under scenarios such as Extreme Weather and Night, where identifying 2D lane features becomes particularly challenging. This is due to our 2D lane queries extracting more comprehensive image information, allowing the 3D queries based on 2D lane prior to better locate lane features in the 3D lane decoder, achieving more accurate predictions of lane point positions.

Table 5: Comparison on topology reasoning task on OpenLane-V2 *subset_A*. The reported results of state-of-art methods are from TopoNet [13].

Method	Backbone	Epoch	OLS \uparrow	DET _l \uparrow	DET _t \uparrow	TOP _u \uparrow	TOP _{tt} \uparrow
STSU [3]	ResNet-50	24e	25.4	12.7	43.0	0.5	15.1
VectorMapNet [20]	ResNet-50	24e	20.8	11.1	41.7	0.4	5.9
MapTR [16]	ResNet-50	24e	26.0	17.7	43.5	1.1	10.4
TopoNet [13]	ResNet-50	24e	35.6	28.6	48.6	4.1	20.3
Topo2D (Ours)	ResNet-50	24e	37.8	29.1	50.6	6.6	21.1

Table 6: Comparison with state-of-art methods on OpenLane validation set.

Method	All	Up & Down	Curve	Extreme Weather	Night	Intersection	Merge & Split
3D-LaneNet [8]	44.1	40.8	46.5	47.5	41.5	32.1	41.7
Gen-LaneNet [9]	32.3	25.4	33.5	28.1	18.7	21.4	31.0
PersFormer [5]	50.5	42.4	55.6	48.6	46.6	40.0	50.7
CurveFormer [1]	50.5	45.2	56.6	49.7	49.1	42.9	45.4
Anchor3DLane [11]	53.7	46.7	57.2	52.5	47.8	45.4	51.2
BEVLaneDet [36]	58.4	48.7	63.1	53.4	53.4	50.3	53.7
LATR [25]	61.9	55.2	68.2	57.1	55.4	52.3	61.5
Topo2D (Ours)	62.6	55.5	67.7	59.1	57.4	52.4	62.5

C Qualitative Results

For the OpenLane-V2 [35] dataset, we visualize the 2D lane detection results for all camera views in Fig. 7. Additionally, to validate the robust performance of our method in topology reasoning task, we visualize lane-lane topology prediction results across more diverse scenarios in Fig. 8. It can be observed that even in highly complex scenarios, Topo2D consistently provides accurate predictions of road topology structures. For the OpenLane [5] dataset, more visualization results are presented in Fig. 9.



Fig. 7: Visualization of 2D and 3D lane detection results on OpenLane-V2 subset_A. Ground truths are showed in red, while predictions are showed in green. Best viewed in color.

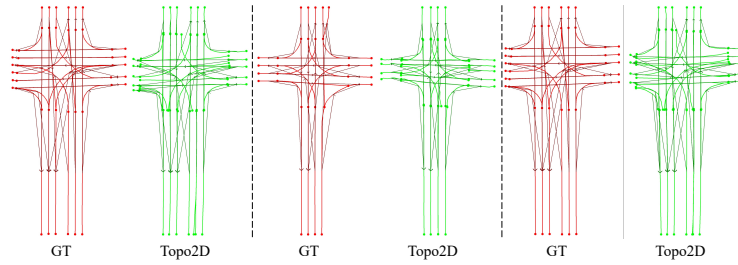


Fig. 8: Visualization of lane-lane topology reasoning results on OpenLane-V2 subset_A. Ground truths are showed in red, while predictions are showed in green. Best viewed in color.

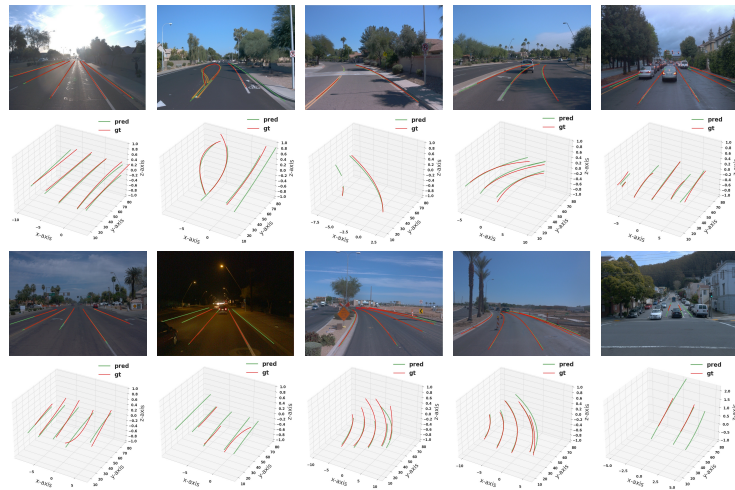


Fig. 9: Visualization under different scenarios on OpenLane validation set.